

# Radiative Effects of Increased Water Vapor Associated with Enhanced Dustiness in the Saharan Air Layer

Claire L Ryder<sup>1</sup>

<sup>1</sup>University of Reading

November 23, 2022

## Abstract

The Saharan Air Layer (SAL) has been shown to be an elevated, well-mixed, warm, dry, frequently dusty layer. The structure of the SAL plays an important role in regional climate and in long-range dust transport. A new analysis of aircraft observations shows that although increased dustiness in the SAL is associated with drier conditions in the lower-SAL as expected, dustiness is also associated with increased moisture in the upper-SAL. We assess the radiative effects of the observed dust and increased water vapor (WV) using a radiative transfer model. The observed WV in the upper-SAL affects the top-of-atmosphere (TOA) direct radiative effect (DRE), while lower-SAL WV affects the surface DRE and column atmospheric heating. TOA DRE is negative for dust-only, while including both the observed dust and WV reduces the magnitude of the negative TOA DRE by 11%. The observed WV structure increases the negative surface DRE from dust by 8% and increases atmospheric heating by 17%. These effects are driven by longwave (LW) radiation, whereby WV changes increase the positive TOA LW DRE by 30%, decrease the surface LW DRE by 52% and change the sign of LW atmospheric heating from negative to positive. The observed WV profile leads to enhanced cooling in the moist upper-SAL and heating in the dry lower-SAL under dustier conditions. Increased WV in the SAL is consistent with other studies demonstrating a trend of increased WV over the Sahara. This work demonstrates the importance of the upper-SAL WV profile in determining the radiative effect dust.

# 1 Radiative Effects of Increased Water Vapor Associated with Enhanced Dustiness in 2 the Saharan Air Layer

3 C.L. Ryder<sup>1</sup>

4 <sup>1</sup>Department of Meteorology, University of Reading, Reading, RG6 6BB, UK.

5 Corresponding author: Claire Ryder ([c.l.ryder@reading.ac.uk](mailto:c.l.ryder@reading.ac.uk))

## 7 Key Points:

- 8 • Observations show enhanced moisture in the upper Saharan Air Layer (SAL) associated  
9 with dust, counter to the conventional dry layer model
- 10 • Enhanced moisture reduces the magnitude of the negative direct radiative effect from  
11 dust at the top of atmosphere by 11%
- 12 • Observed water vapor structure leads to enhanced cooling in the moist upper-SAL and  
13 heating in the dry lower-SAL under dustier conditions

## 15 Abstract

16 The Saharan Air Layer (SAL) has been shown to be an elevated, well-mixed, warm, dry,  
17 frequently dusty layer. The structure of the SAL plays an important role in regional climate and  
18 in long-range dust transport. A new analysis of aircraft observations shows that although  
19 increased dustiness in the SAL is associated with drier conditions in the lower-SAL as expected,  
20 dustiness is also associated with increased moisture in the upper-SAL. We assess the radiative  
21 effects of the observed dust and increased water vapor (WV) using a radiative transfer model.

22 The observed WV in the upper-SAL affects the top-of-atmosphere (TOA) direct radiative effect  
23 (DRE), while lower-SAL WV affects the surface DRE and column atmospheric heating. TOA  
24 DRE is negative for dust-only, while including both the observed dust and WV reduces the  
25 magnitude of the negative TOA DRE by 11%. The observed WV structure increases the negative  
26 surface DRE from dust by 8% and increases atmospheric heating by 17%. These effects are  
27 driven by longwave (LW) radiation, whereby WV changes increase the positive TOA LW DRE  
28 by 30%, decrease the surface LW DRE by 52% and change the sign of LW atmospheric heating  
29 from negative to positive. The observed WV profile leads to enhanced cooling in the moist  
30 upper-SAL and heating in the dry lower-SAL under dustier conditions. Increased WV in the  
31 SAL is consistent with other studies demonstrating a trend of increased WV over the Sahara.  
32 This work demonstrates the importance of the upper-SAL WV profile in determining the  
33 radiative effect dust.

## 34 Plain Language Summary

35 During summer, warm, dry, dusty air is transported from the Sahara across the Atlantic Ocean in  
36 an elevated plume. This plume has many impacts on climate, such as suppressing convection  
37 which may be important to hurricane development, and transporting dust particles which can  
38 supply nutrients to the oceans and degrade respiratory health. Previously the plume has been  
39 found to be very dry, but by using new observations from a research aircraft, we show that high

40 levels of moisture are found at its top. This is important because it alters the balance of heating  
41 and cooling at different altitudes within the atmosphere, which has not been accounted for in this  
42 way before, and may impact how Saharan air interacts with weather in the Atlantic region and  
43 how easily dust is transported over long distances. We find that the addition of moisture at the  
44 top of the plume adds a warming of 11% compared to the effects from dusty air, and decreases in  
45 moisture at lower altitudes can change the nighttime effect of the plume from cooling to heating.  
46 Therefore future work should take into account the vertical distribution moisture in Saharan dust  
47 plumes as well as the dust itself.

## 48 **1 Introduction**

49 The Saharan Air Layer (SAL) is conventionally considered to be a deep warm, dry, elevated  
50 layer of air which exists over the tropical north Atlantic Ocean from late spring to early fall,  
51 frequently containing mineral dust transported from North Africa (Braun, 2010). The SAL  
52 originates from strong surface heating over the Sahara desert, where a deep, well-mixed, warm,  
53 dry boundary layer develops, typically extending up to 5 to 6 km, known as the Saharan  
54 Boundary Layer (Engelstaedter et al., 2015; Marsham et al., 2013). The SAL, and any embedded  
55 mineral dust, is transported westwards by prevailing winds and steered by African Easterly  
56 Waves. As it moves over the Atlantic Ocean, it is undercut by a moist marine boundary layer  
57 (MBL), forming an elevated mixed layer known as the SAL, characterized by near-constant  
58 potential temperatures and water vapor (WV) mixing ratios, and retaining its structure as it is  
59 transported westwards (Carlson, 2016; Dunion & Velden, 2004).

60  
61 In the original conceptual model of the SAL (e.g. (Carlson & Prospero, 1972; Dunion, 2011;  
62 Karyampudi et al., 1999; Prospero & Carlson, 1972) the SAL is shown to be warm, dry and to  
63 varying degrees, dust laden. For example, reported values of WV mixing ratios within the  
64 eastern SAL are around 2 to 5 g/kg (Carlson & Benjamin, 1980; Carlson & Prospero, 1972;  
65 Ismail et al., 2010; Karyampudi et al., 1999), and 1 to 6 g/kg in the western SAL (Dunion, 2011;  
66 Dunion & Velden, 2004). Kanitz et al. (2014) present measurements across the width of the  
67 tropical Atlantic, finding WV mixing ratios between 3 to 7 g/kg within the SAL. Warm, dry  
68 anomalies in the SAL between 800 to 900 hPa have been shown to be related to increased dust  
69 optical depth. Together the dusty, dry anomalies are responsible for heating the lower SAL and  
70 maintaining the temperature inversion its base, as well has playing a role in suppressing deep  
71 convection and increasing low cloud fraction (Doherty & Evan, 2014; Wong & Dessler, 2005;  
72 Wong et al., 2009).

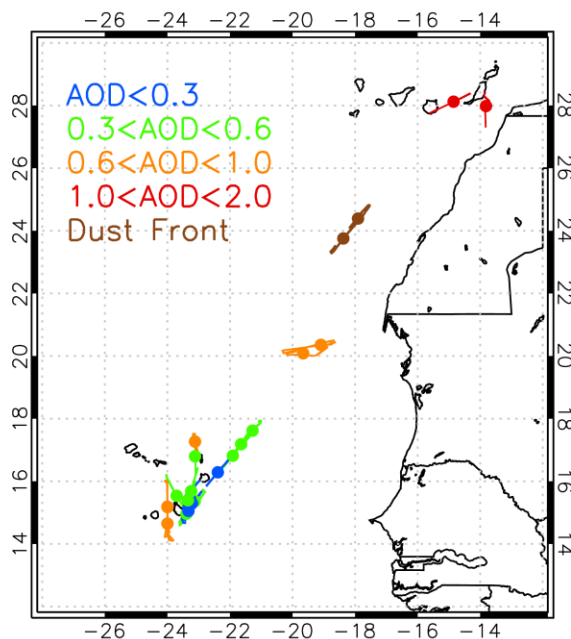
73  
74 Around 50% of dust events in the summertime Sahara are driven by cold pool outflows  
75 (haboobs), with the dust being associated with elevated moisture levels deriving from moist  
76 downdrafts (Marsham et al., 2013; Marsham et al., 2008). Several studies have described the role  
77 of cold pool outflows and density currents in transporting dust and moisture into the arid Sahara  
78 (Allen et al., 2013; Engelstaedter et al., 2015; Flamant et al., 2007). Marsham et al. (2016)  
79 examined the relative radiative effects of dust and WV in the Saharan heat low (SHL), finding  
80 that WV variations exert a dominant role on the top of atmosphere (TOA) radiation budget,  
81 while dust variability was dominant in driving atmospheric heating and surface radiation.  
82 Gutleben et al. (2019) found that SAL WV mixing ratios over the western Atlantic for one dust  
83 event were elevated compared to those in the surrounding free atmosphere, and found that the  
84 altered WV profile within the dust led to substantial changes in radiative heating rates.

85  
 86 Here we examine dust and WV aircraft observations in the tropical north Atlantic Ocean region.  
 87 During research flights, it was noticed that specific humidity often increased when dust layers  
 88 were penetrated, and was particularly noticeable during a few extremely large dust events  
 89 (Marengo et al., 2018). Since this increased moisture within the dusty SAL is counter to the  
 90 conventional model of a dry, dusty SAL, here we examine the evidence from airborne  
 91 observations and evaluate the radiative effect of the observed changes in dust and enhanced  
 92 water vapor.  
 93

## 94 2 Methods

### 95 2.1 Aircraft Observations

96 We present meteorological and aerosol in-situ aircraft observations from the AERosol Properties  
 97 – Dust (AER-D) airborne field campaign (Marengo et al., 2018) which took place during August  
 98 2015 in the region of the Cape Verde Islands (Figure 1). The Facility for Atmospheric Airborne  
 99 Measurements BAe146 research aircraft sampled a series of dust events in the SAL between 7  
 100 and 25 August 2015, described in more detail by Ryder et al. (2018), Liu et al. (2018), Marengo  
 101 et al. (2018), where microphysical, chemical, optical and radiative properties of the dust samples  
 102 are presented.  
 103



104  
 105 **Figure 1:** Locations of AER-D aircraft profiles analysed in this study. Lines show locations  
 106 sampled during profile ascents or descents, solid dots indicate mean profile location. Colors  
 107 indicate AOD as shown in the legend.

108  
 109 Here we use in-situ observations from 24 aircraft profile descents and ascents as shown in Figure  
 110 1, sampled during 6 flights (also shown in Ryder et al. (2018), their table 2). Profiles cover  
 111 altitudes from close to the ocean surface to above the SAL, generally ~5.5 km. All the dust

112 events sampled during AER-D were driven by outflows from mesoscale convective systems  
113 ('haboobs,' identified in Ryder et al. (2018), which in most cases were mixed vertically  
114 throughout the Saharan boundary layer by convective mixing before being advected over the  
115 ocean in an elevated SAL. However, two flights (b923, b924) sampled a large dust plume with  
116 aerosol optical depths (AODs) at 550 nm greater than 1, further to the north close to the Canary  
117 Islands. Two particular profiles sampled an extremely unusual dust structure with very high dust  
118 concentrations peaking at low altitudes of around 1 km, constituting a clear 'dust front' which  
119 kept its structure (low altitude, intense dust concentrations) while being advected out over the  
120 Atlantic Ocean (brown lines in Figure 1). This event is investigated in more detail by Marengo et  
121 al. (2018), and is referred to here as the 'dust front' case since it is different to the other, more  
122 typical elevated dust profiles sampled.

123  
124 Airborne measurements of temperature are taken from a Rosemount/Goodrich type 102 Total Air  
125 Temperature probe, using the non-deiced models for all flights except b934 when data is not  
126 available, and when the deiced model was used instead. Dew point temperature measurements,  
127 used to calculate water vapor mixing ratios are taken from the Sky Phys Tech Inc. Nevzorov  
128 total water content probe (Korolev et al., 1998), except for flights b923, b934 and b932 Profile 1  
129 where they are taken from the General Eastern 1011B Chilled Mirror Hygrometer. Pressure was  
130 measured by a reduced vertical separation minimum data system.

131  
132 Ryder et al. (2018) have shown that the aerosol load sampled was predominantly mineral dust,  
133 including the aerosol in the marine boundary layer. Here we take a straightforward indication of  
134 dust loading from the dust extinction at 550 nm, calculated by summing dust scattering and  
135 absorption. Scattering is measured by a TSI 3563 integrating nephelometer (550 nm wavelength  
136 used here) and absorption measurements were made by a Radiance Research particle soot  
137 absorption photometer (PSAP) at 567 nm. Further details and processing information can be  
138 found in Ryder et al. (2018). Extinction is integrated vertically from aircraft profiles to provide  
139 AODs at 550 nm.

140  
141 **2.2 Radiative Transfer Calculations**

142 We employ the Suite Of Community RAdiative Transfer codes based on Edwards and Slingo  
143 (SOCRATES, Edwards and Slingo (1996), Manners et al. (2017)) radiative transfer model  
144 (RTM) in order to calculate radiative fluxes. SOCRATES is the RTM implemented by the family  
145 of UK Met Office numerical weather prediction and climate models. Here we use the spectral  
146 setup analogous to that from HadGEM3 model Global Atmosphere 6 configuration (Walters et  
147 al., 2011). A two stream practical improved flux method is used (Zdunkowski et al., 1980).

148  
149 Shortwave fluxes are calculated over 6 spectral bands from 0.2 to 10  $\mu\text{m}$  and longwave fluxes  
150 are calculated in 9 spectral bands from 3.3 to 100  $\mu\text{m}$ . Gaseous absorption is represented  
151 according to Cusack et al. (1999) using a correlated-k method. Water vapor terms are based on  
152 the HITRAN 2001 database (Rothman et al., 2003) for gaseous absorption coefficients, with  
153 updates up to 2003. The water vapor continuum is represented using version 2.4 of the CKD  
154 model. Top of atmosphere incoming solar radiation is set to  $1365 \text{ Wm}^{-2}$ .

155  
156 SOCRATES requires aerosol vertical profiles in terms of mass mixing ratios. These are  
157 calculated to represent dust from the measured in-situ aerosol extinction profiles, converted to a

158 mass loading by using a field campaign specific mass extinction coefficient of  $0.36 \text{ m}^2\text{g}^{-1}$  (Ryder  
159 et al., 2018). This value represents the full size distribution up to  $100 \mu\text{m}$  diameter.

160  
161 We use 122 vertical levels in SOCRATES, covering 1007 to 0.0005 hPa, with resolution  $\sim 20$   
162 hPa in the lower atmosphere, including the SAL. Observations of dust mass mixing ratio, water  
163 vapor mixing ratio and temperature are regridded to the required vertical grid. Only dust aerosols  
164 are included. At altitudes above where aircraft data were measured, dust concentrations are set to  
165 zero and temperature and water vapor values are set to revert to values from a tropical standard  
166 profile (Anderson et al., 1986). Ozone, methane, carbon monoxide, carbon dioxide, nitrous oxide  
167 and oxygen profiles are taken from Randles et al. (2012). Shortwave surface albedo is set to 0.05  
168 representative of an ocean surface and LW surface emissivity to 0.982 in all spectral intervals.

169  
170 Dust optical properties are calculated spectrally in the longwave (LW) and shortwave (SW)  
171 spectra using lognormal size distribution parameters representing the AER-D SAL average, as  
172 given in Ryder et al. (2018). In the SW, complex refractive index data are taken from Colarco et  
173 al. (2014) and LW values from Volz (1973) since these datasets fall centrally in the range from  
174 literature (Ryder et al., 2019) and cover the full spectral range required. Mie scattering code (and  
175 therefore a spherical particle assumption) is used to calculate spectral optical properties of mass  
176 extinction coefficient, single scattering albedo (SSA) and asymmetry parameter, which are  
177 applied in SOCRATES and are shown in Table 1. The SSA at visible wavelengths is 0.86,  
178 considerably lower than the AER-D campaign mean value of 0.95 at 550 nm (Ryder et al., 2018).  
179 The difference occurs due to the spectral averaging applied here which incorporates absorption  
180 increasing significantly towards smaller solar wavelengths, as well as the use of the Colarco et  
181 al. (2014) imaginary refractive index of 0.0024 at 550 nm compared to a value of 0.0010 derived  
182 in Ryder et al. (2018). SOCRATES includes both absorption and scattering in the LW spectrum.

183

Spectral Range	Lower wavelength, $\mu\text{m}$	Upper wavelength, $\mu\text{m}$	MEC/ $\text{m}^2\text{g}^{-1}$	SSA	Asymmetry Parameter
SW	0.20	0.32	0.36	0.70	0.83
	0.32	0.69	0.36	0.86	0.76
	0.69	1.19	0.36	0.95	0.71
	1.19	2.38	0.35	0.93	0.69
	2.38	10.00	0.26	0.82	0.71
LW	25.0	10000.0	0.05	0.28	0.29
	18.2	25.0	0.15	0.36	0.32
	12.5	18.2	0.13	0.42	0.52
	13.3	16.9	0.10	0.37	0.54
	8.3	12.5	0.17	0.42	0.56
	8.9	10.1	0.28	0.45	0.46
	7.5	8.3	0.09	0.41	0.74
	6.7	7.5	0.16	0.62	0.72
	3.3	6.7	0.24	0.87	0.68

184 **Table 1:** Optical properties applied in SOCRATES for each spectral band estimated using  
185 refractive index data from Colarco et al. (2014) for the SW, Volz et al. (1973) for the LW and the  
186 AER-D mean size distribution (Ryder et al., 2018).

187 Sensitivity tests have also been carried out using more and less absorbing dust at solar  
 188 wavelengths. These were calculated using the more absorbing OPAC dataset refractive indices  
 189 with the OPAC transported mineral dust size distribution (Hess et al., 1998), and the less  
 190 absorbing refractive index dataset of Balkanski et al. (2007) combined with a smaller dust size  
 191 distribution (Dubovik et al., 2002). At infrared wavelengths, sensitivity to dust is tested by  
 192 varying the dust size distribution to the smaller one of Dubovik et al. (2002) and the refractive  
 193 index to that from OPAC. These calculations yield SSA values of 0.74 and 0.94 for the more and  
 194 less absorbing cases respectively for the spectral band spanning wavelengths of 0.32 to 0.69  
 195 microns.

196  
 197 Surface temperatures for the LW calculations are set based on values observed from aircraft in-  
 198 situ observations or dropsondes. SW diurnal averages are calculated by running SOCRATES at  
 199 three solar zenith angles based on the location and time of year of observations, which are  
 200 multiplied by a gaussian weight and summed.

201  
 202 For each of 24 profiles, 4 radiative transfer simulations are conducted, as outlined in Table 2, in  
 203 order to isolate the effects of the altered WV profile in the SAL, the presence of dust, and their  
 204 combined effect. The temperature profile is always taken from aircraft measurements. For the  
 205 CONTROL, no radiative effects of dust are included. In order to create a WV profile  
 206 representative of background conditions for the region for the control, a median of the aircraft  
 207 WV profiles where AOD is less than 0.3 is taken (blue lines in fig 1e and 2a), which represents a  
 208 non-SAL background WV profile. We do not use the tropical standard WV profile (Anderson et  
 209 al., 1986), because the non-SAL atmosphere in the region is significantly moister than this (see  
 210 Figure 1e). The three perturbation experiments shown in Table 2 allow the quantification of the  
 211 radiative impacts relative to a typical background, non-dusty state in the region. For the dust only  
 212 experiment (DU), dust observations from aircraft measurements are included, but the  
 213 background WV profile maintained, such that only the radiative impact of dust is assessed. For  
 214 the water vapor only experiment (WV), no dust is included, but the water vapor profile used is  
 215 taken from the aircraft observations. Finally, for DU+WV, both the aircraft-observed dust and  
 216 water vapor profiles are included to assess their combined effect. For each experiment, vertical  
 217 profiles of SW and LW radiative fluxes and heating rates are calculated for all aircraft profiles.

218  
 219  
 220

Experiment Name	Abbreviation	Temperature Profile	Dust Profile	Water Vapor Profile
Control	CONTROL	Aircraft observations	None	Background WV profile: median of WV profiles where AOD<0.3
Dust only	DU	Aircraft observations	Aircraft observations	Background WV profile: median of WV profiles where AOD<0.3
Water vapor only	WV	Aircraft observations	None	Aircraft observations
Dust and water vapor	DU+WV	Aircraft observations	Aircraft observations	Aircraft observations

221 **Table 2:** SOCRATES experiments. Each experiment is performed for each of 24 aircraft  
 222 profiles.

223 The direct radiative effect (DRE) due to each experiment relative to the control is calculated as  
 224 defined in equation 1.

$$DRE_{lev}^{spect} = NET\_EXPT_{lev}^{spect} - NET\_CONTROL_{lev}^{spect}$$

225 **Equation 1**

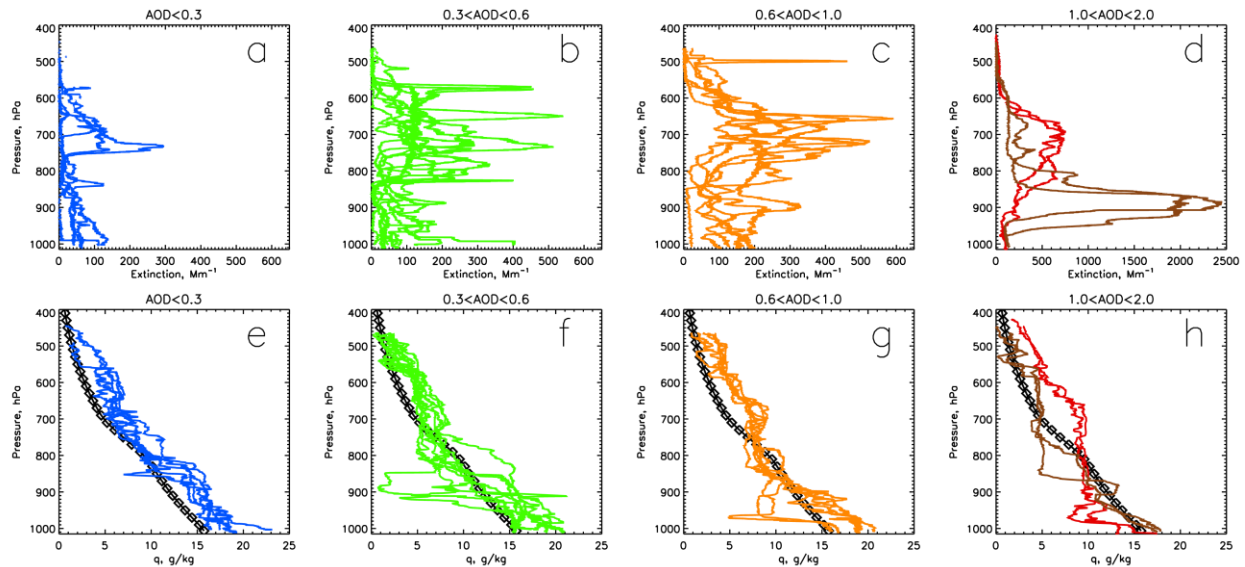
226 NET refers to the net (downwards minus upwards) radiative flux at a level (lev) either at the top  
 227 of atmosphere (TOA) or surface (SFC), for spect which can be either the SW spectrum, LW  
 228 spectrum, or total (SW+LW). EXPT refers to the experiment in question, either DU, WV or  
 229 DU+WV. DREs calculated are instantaneous, diurnally averaged calculations. Positive values at  
 230 the TOA indicate a warming of the earth atmosphere system. The atmospheric (ATM) radiative  
 231 effect, also sometimes referred to as atmospheric radiative convergence and indicating  
 232 atmospheric column heating when positive, is calculated from  $DRE_{ATM}^{spect} = DRE_{TOA}^{spect} -$   
 233  $DRE_{SFC}^{spect}$ .

### 234 3 Results

#### 235 3.1 Aircraft observations of dust and water vapor

236 Figure 2 shows the profiles of aerosol extinction and water vapor observed by the aircraft. Each  
 237 is subset by the measured AOD, selected so that each range contains a reasonable number of  
 238 profiles. The dust load is clearly be seen to increase as AOD increases, and the expected vertical  
 239 profile of the SAL develops, with (mostly) enhanced dust centered around 700 hPa.  
 240

241 Water vapor profiles are also shown. It is evident that even in cases without much dust  
 242 (AOD<0.3, blue), the atmosphere is moister than the tropical standard. This is perhaps not  
 243 surprising given the large amount of variability across tropical regions for which the tropical  
 244 standard atmosphere represents (e.g. Dunion (2011)).  
 245  
 246



248 **Figure 2.** Aircraft profile observations of aerosol extinction (top row) and water vapor mixing  
 249 ratio (bottom row). Each variable is subset by measured AOD: blue (AOD<0.3, 5 profiles), green  
 250 (0.3<AOD<0.6, 9 profiles), orange (0.6<AOD<1.0, 6 profiles) and red (AOD>1.0, 4 profiles).  
 251 Brown lines indicate dust front event. Note that panel (d) extinction x-axis is nearly 5 times as  
 252 large as (a)-(c). Black diamonds indicate the tropical standard profile. WV profiles shown in  
 253 panel e are used to create the background WV profile as in Table 2 for the CONTROL  
 254 experiment.

255 As AOD increases, the encroachment of the SAL is evident with a deepening of the elevated,  
 256 well-mixed layer. This can also be seen in Figure 3 where medians for each AOD category, and  
 257 anomalies relative to the background state are shown. As AOD increases, a well-mixed layer of  
 258 near-constant potential temperature and water vapor develop, as expected. The well-mixed  
 259 nature of the SAL means that at lower altitudes, the SAL is warmer and drier than the  
 260 background state, whereas towards the top of the SAL the atmosphere is cooler and moister than  
 261 the background state.

262  
 263 Figure 3b clearly shows that under increased AODs (or dust loading), enhanced WV in the  
 264 upper-SAL and decreased WV in the lower-SAL is observed. This becomes more pronounced as  
 265 the AOD increases. For AODs over 0.6, enhanced WV is observed for heights above 750 hPa,  
 266 with anomalies exceeding 2 g/kg for the 1<AOD<2 category (red line). An interesting double-  
 267 peaked water vapor anomaly structure is seen, whereby anomalies peak at a lower level of  
 268 around 700 hPa, coincident with the center of the SAL and the anomalies it brings, but anomalies  
 269 also peak at around 500 hPa, due to the dustier SAL cases extending deeper vertically with more  
 270 moisture at higher altitudes.

271  
 272 Dust extinction (Figure 3e) and potential temperature (Figure 3c) as a function AOD are also  
 273 shown, and show the well-mixed and relatively warmer structure of the SAL becoming more  
 274 clearly defined as it becomes dustier, as expected. It is also notable that the highest AOD  
 275 category (red) shows a cold anomaly in the upper SAL, at heights above 520 hPa.

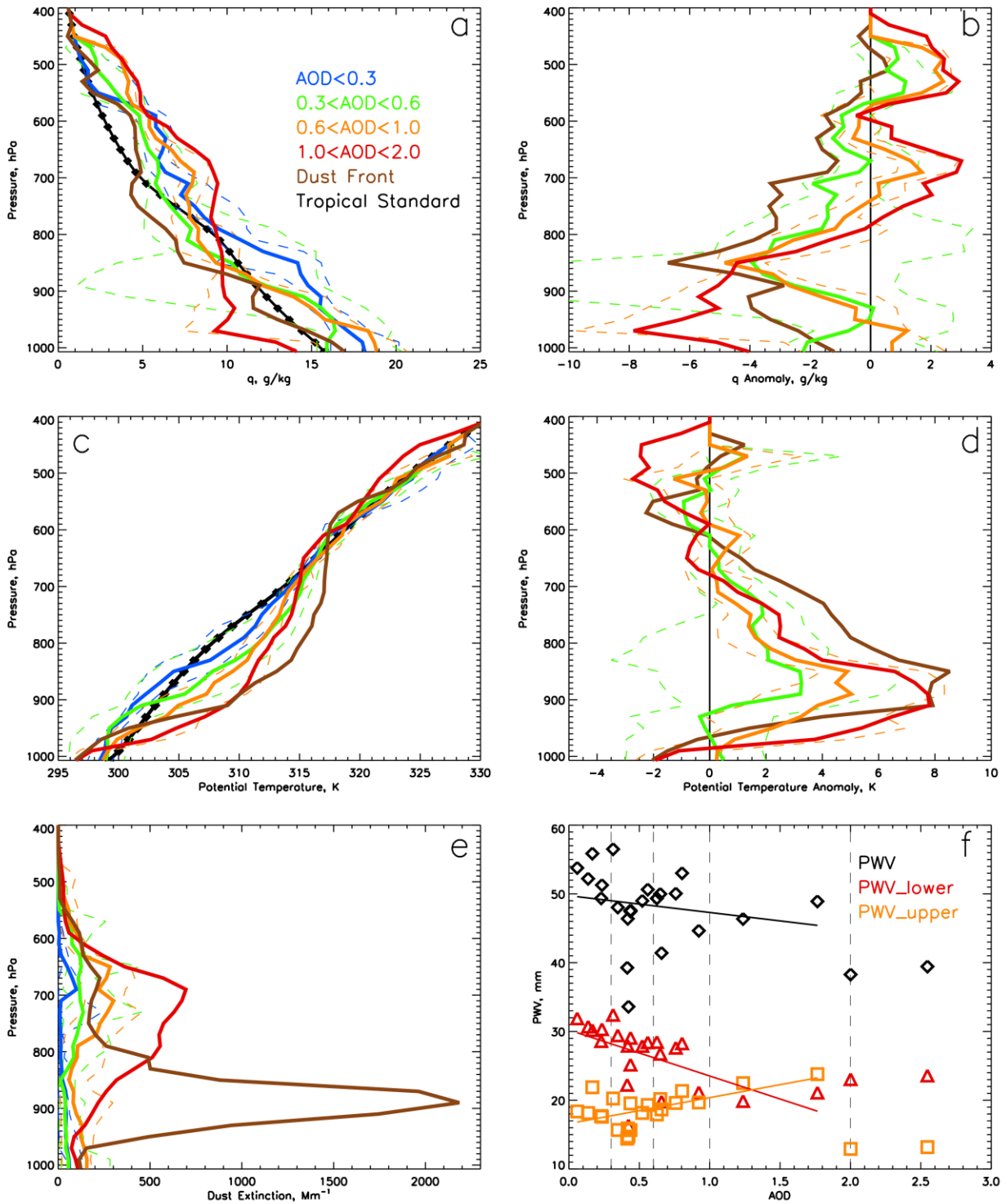
276  
 277 The case of the dust front, shown in brown in Figures 2 and 3, is particularly interesting. The  
 278 extremely high dust loadings are reflected by extinction values of up to nearly 2500  $\text{Mm}^{-1}$ ,  
 279 peaking at around 900 hPa (~1km), unusually low altitudes for a dust event over the tropical  
 280 north Atlantic during summer. The figures show that the peak in dust loadings at ~900 hPa are  
 281 coincident with an increase in WV content (Figure 2h) up to around 13 g/kg relative to the more  
 282 well-mixed layer above this with WV mixing ratios of around 5 g/kg. Ryder et al. (2018) and  
 283 Marenco et al. (2018) have identified this dust event as being an intense haboob which  
 284 propagated out over the Atlantic at low altitudes, rather than being mixed vertically through the  
 285 Saharan boundary layer first, as usually occurs. Thus the intense concentration of high moisture  
 286 and dust loadings at low altitudes can be traced back to cold-pool outflow driving the dust uplift  
 287 in the form of a recent haboob.

288  
 289 Figure 3f shows the relationship between AOD and precipitable water vapor (PWV) for the  
 290 whole column (black), for the lower SAL (PWV\_lower, p>820 hPa, red), and for the upper SAL  
 291 (PWV\_upper, pressure from 780 to 480 hPa, orange). Overall, as AOD increases, PWV  
 292 decreases, though there is a large amount of variability and the linear fit has a low correlation  
 293 (0.18). More insight is gained into the impact of increased dust through viewing the SAL lower

294 and upper WV changes separately. Figure 3f shows that as AOD increases, PWV\_upper  
295 increases by 3.8 mm per unit AOD, while PWV\_lower decreases by 6.7 mm per unit AOD, with  
296 the linear fits showing correlations of 0.58 and 0.59 respectively. For the upper-SAL,  
297 PWV\_upper increases from 18 mm to 23 mm between the AOD categories of  $AOD < 0.3$  and  
298  $1 < AOD < 2$  respectively for the profiles shown in Figure 2a (blue vs red). Therefore there is a  
299 clear relationship between increased dust load (AOD), decreased lower-SAL moisture, and  
300 increased upper-SAL moisture.

301  
302 Note that the two highest AOD data points (relating to the dust front case) can be viewed to some  
303 extent as outliers and are not included in the linear fits. As Figure 3f shows, the two in-situ  
304 aircraft profiles sampling this dust front feature demonstrate low PWV\_upper and high  
305 PWV\_lower values, different to the trend demonstrated by the more conventional elevated SAL  
306 structure of the other profiles.

307



308  
 309 **Figure 3.** Aircraft observations of (a) water vapor mixing ratio, (c) potential temperature and (e)  
 310 aerosol extinction; anomalies of (b) water vapor mixing ratio and (d) potential temperature  
 311 relative to the background state (profiles where AOD < 0.3). Profiles are regridded vertically as  
 312 applied in the RTM. Profiles are grouped by AOD range as indicated with bold lines indicating  
 313 the median and dashed lines the 10<sup>th</sup> and 90<sup>th</sup> percentile ranges for AOD categories where  
 314 AOD < 1. 1 < AOD < 2 and dust front categories (red and brown) are represented by means as

315 categories contain only 2 profiles. Black line with symbols indicates tropical standard profile. (f)  
316 Relationship for all individual profiles between AOD and PWV, PWV\_lower (pressure >820  
317 hPa) and PWV\_upper (480 hPa < pressure < 780 hPa), and linear fits where AOD < 2, with  
318 Pearson's correlation coefficients of 0.18, 0.58 and 0.59, and dPWV/dAOD values of -2.4, -6.7  
319 and +3.8 mm/AOD respectively.

320  
321 Although the structure of the SAL has been extensively examined and documented, some of the  
322 changes found here are not consistent with the conventional view of the SAL's structure. Figures  
323 2 and 3 show much moister values than those documented in most cases, up to 11 g/kg  
324 depending on altitude, and with a clear upper SAL moistening with increasing dustiness relative  
325 to less dusty cases. Previously, the radiative roles of dust and *dry* SAL air have been assessed  
326 (e.g. Wong et al., 2009). Next, we evaluate the radiative effects of the measured dust, and *moist*  
327 upper SAL air shown in the observations.

328

### 329 **3.2 Impact of altered WV structure on Radiative Effect**

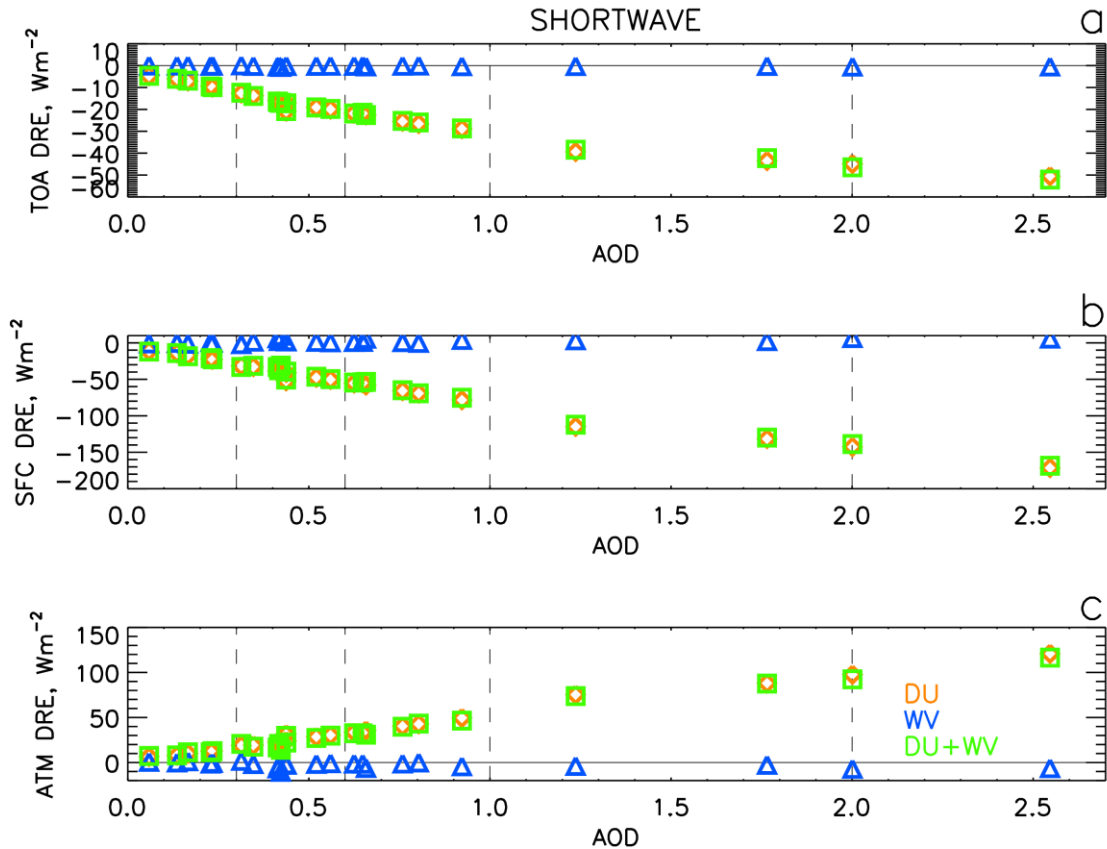
330 Having demonstrated that increased dust loadings were associated with increased upper-SAL  
331 WV (PWV\_upper) but decreased lower-SAL WV (PWV\_lower) during AER-D, the DREs from  
332 dust only, WV only and both combined are now described in order to investigate the radiative  
333 impact of the WV changes relative to those from the dust.

334

335 Figure 4 shows the shortwave DRE as a function of AOD for each experiment at the TOA,  
336 surface and for the atmospheric column. DREs are relative to the CONTROL experiment, where  
337 WV is derived from conditions where AOD < 0.3. The results show that in the shortwave  
338 spectrum, the main driver of the DRE is always dust, since the WV DREs are comparatively  
339 small. Increased dust AOD leads to a more negative TOA DRE, a more negative surface DRE,  
340 and larger atmospheric heating.

341

342

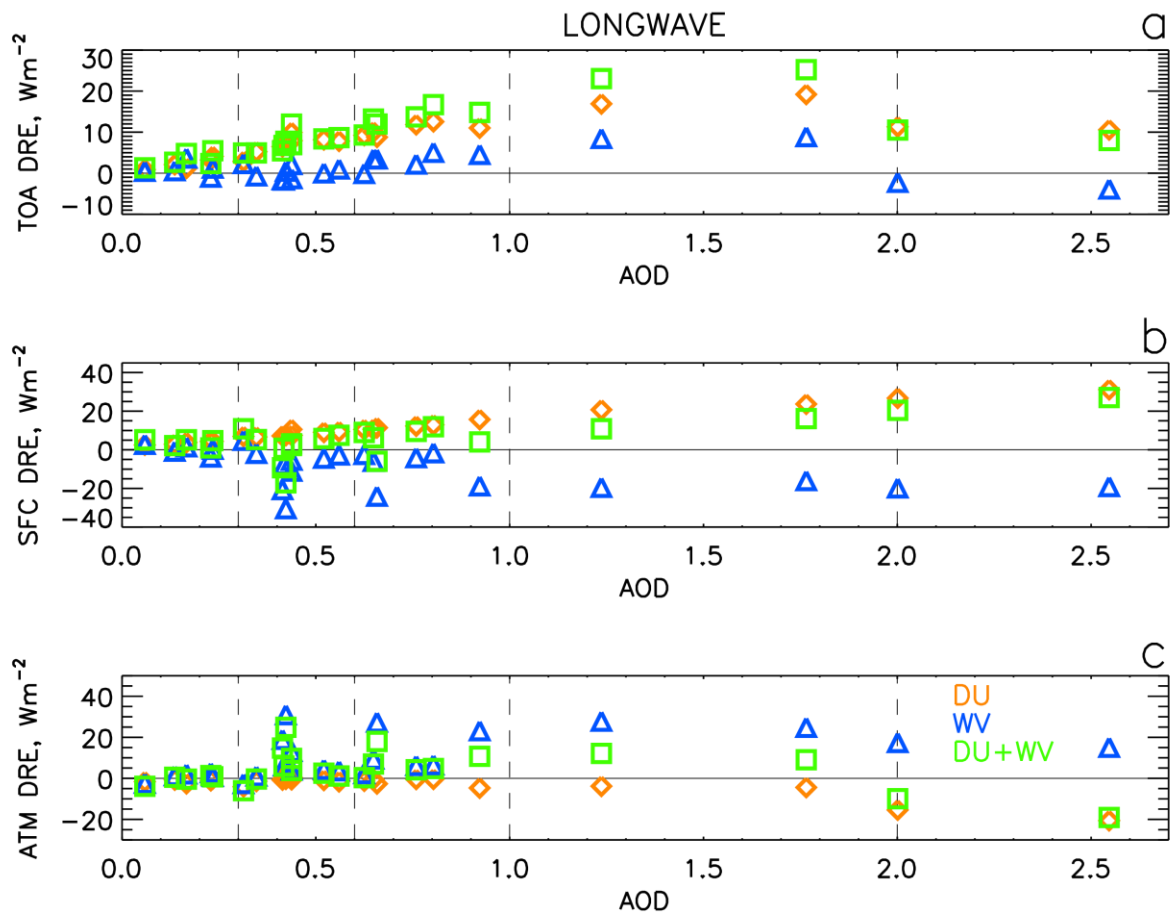


343  
 344 **Figure 4.** Shortwave DRE relative to control experiment for the inclusion of dust only (DU,  
 345 orange), WV only (blue) and dust and WV (DU+WV, green), as a function of 550 nm AOD.  
 346 Panels show (a) DRE at the TOA, (b) surface and (c) atmospheric column. Vertical dashed lines  
 347 indicate AOD categories.

348 Figure 5 shows DREs as a function of AOD, but for the longwave spectrum. Here, the WV DRE  
 349 exerts a large enough effect to alter the DRE significantly. At the TOA dust generates a positive  
 350 LW DRE (orange points), which increases with AOD. (The exception are the two ‘dust front’  
 351 cases with the highest AOD, where the dust was lower in the atmosphere resulting in weaker LW  
 352 DREs). The WV TOA DRE is also mostly positive and also increases with AOD (blue data  
 353 points). This is consistent with increased WV, as observed in the upper-SAL, and will be  
 354 investigated further in Section 3.3. As a result of the positive DRE due to WV, the DU+WV LW  
 355 TOA DRE (green data points) is significantly larger than due to dust only, with values increasing  
 356 by an average of 30% and a wide range of -27% to 292%.

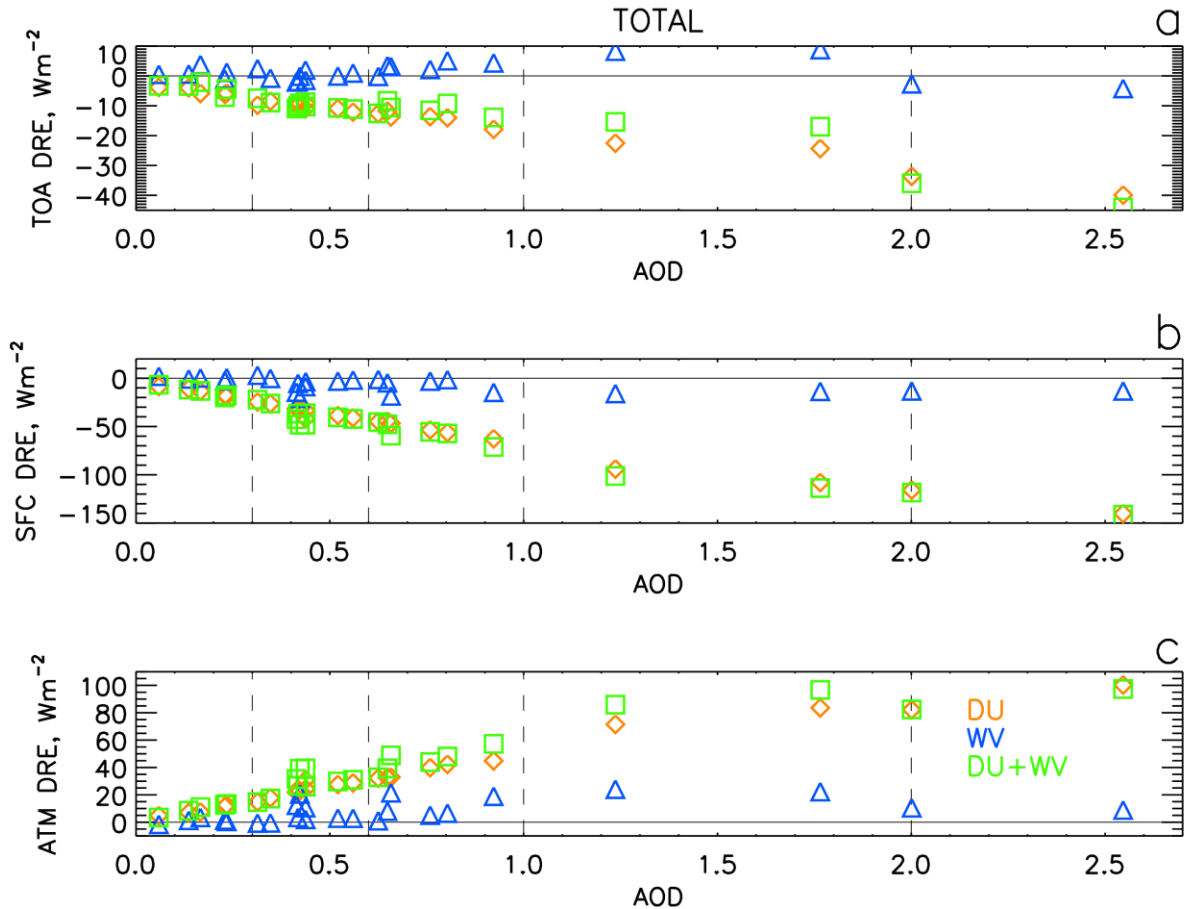
357  
 358 At the surface and through the atmospheric column, dust causes a surface warming and an  
 359 atmospheric cooling. The WV DRE is the opposite, resulting in a negative surface DRE and  
 360 atmospheric heating. This is consistent with a net reduction in WV, and Section 3.3 will  
 361 demonstrate that these changes are driven by a reduction in lower-SAL WV. At the surface, this  
 362 results in a reduced LW DRE from DU+WV compared to DU alone, with values reducing by  
 363 52% on average. In the atmosphere, WV changes the sign of atmospheric heating, from a mean  
 364 of  $-1.5 Wm^{-2}$  for DU to  $5.5 Wm^{-2}$  for DU+WV. This could influence SAL dynamics at nighttime  
 365 when shortwave influences are inactive.

366



367  
 368 **Figure 5.** Longwave DRE relative to control experiment for the inclusion of dust only (DU,  
 369 orange), WV only (blue) and dust and WV (DU+WV, green), as a function of 550 nm AOD.  
 370 Panels show (a) DRE at the TOA, (b) surface and (c) atmospheric column. Vertical dashed lines  
 371 indicate AOD categories.

372 Figure 6 shows the total (SW+LW) DREs as a function of AOD, and demonstrates how the dust  
 373 and WV shortwave and longwave impacts from Figures 4 and 5 combine. The total TOA DRE  
 374 for dust is negative, reflecting the larger magnitude originating from the SW dust DRE compared  
 375 to the LW. WV TOA DREs are positive, driven by the LW DRE from WV. The net effect of  
 376 including the observed WV profiles is to reduce the total negative DRE for DU+WV compared  
 377 to DU alone. Overall including WV effects (excluding the dust front case) increases the TOA  
 378 DRE from dust by  $-1.5$  to  $7.3 \text{ Wm}^{-2}$  (mean of  $1.3 \text{ Wm}^{-2}$ ) or increases the negative DRE by  $-17$  to  
 379  $64\%$  (mean of  $11\%$ ).



380  
 381 **Figure 6.** Total (shortwave plus longwave) DRE relative to control experiment for the inclusion  
 382 of dust only (DU, orange), WV only (blue) and dust and WV (DU+WV, green), as a function of  
 383 550 nm AOD. Panels show (a) DRE at the TOA, (b) surface and (c) atmospheric column.  
 384 Vertical dashed lines indicate AOD categories.

385 Figure 6 shows that at the surface, the main driver of the total DRE is dust, where the large  
 386 negative SW DREs are slightly reduced in magnitude by positive values from the LW spectrum.  
 387 WV DREs at the surface are small and negative and reduce the SFC DRE by a mean of 8% for  
 388 DU+WV compared to DU. In the atmospheric column, dust is also the main driver of  
 389 atmospheric heating, originating from large positive SW values shown in Figure 3. However,  
 390 here the WV change can act to enhance this heating from -1 to  $16 \text{ Wm}^{-2}$  (mean of  $5 \text{ Wm}^{-2}$  or  
 391 17%), as a result of the LW WV effect.

392

### 393 3.3 Impact of WV in the lower and upper-SAL

394 Figure 7 and Figure 8 show the LW DREs as a function of PWV in the lower-SAL and upper-  
 395 SAL respectively, to isolate the impacts of the changed WV structure with increasing dust,  
 396 whereby WV in the upper-SAL increases, but decreases in the lower-SAL.

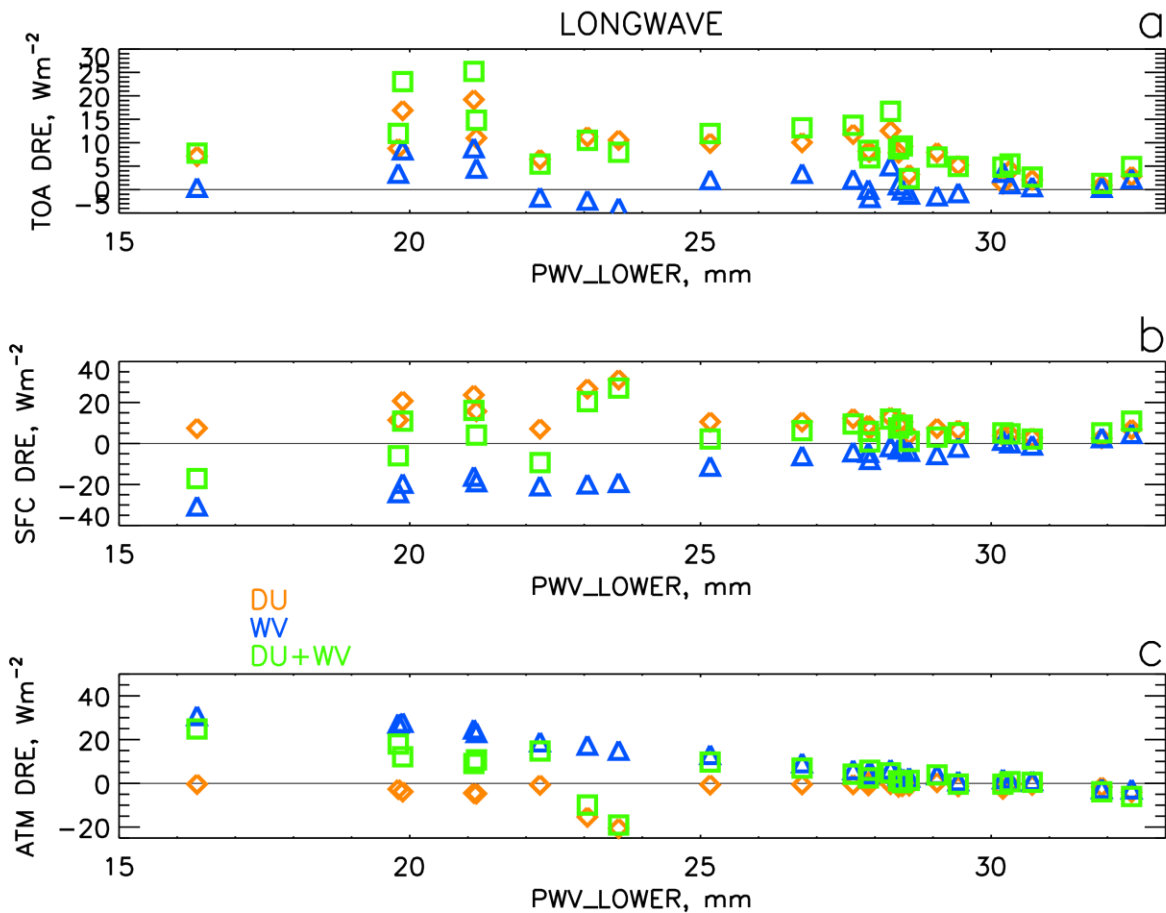
397

398 In Figure 7, clear relationships between PWV\_lower and both surface and atmospheric LW DRE  
 399 can be seen for water vapor (blue data points). In the atmosphere (panel c), a drier lower-SAL  
 400 results in relatively more atmospheric heating (or equivalently less atmospheric cooling), while

401 at the surface, drier lower-SAL conditions result in a more negative LW DRE because less  
 402 radiation is emitted downwards by the drier atmosphere.

403  
 404 Under dustier conditions when the lower-SAL is drier, the DU experiment mostly results in  
 405 slightly negative ATM DRE values (atmospheric cooling, orange points in Figure 7c). The  
 406 addition of the WV DRE changes are large enough to change the sign of ATM DRE and result in  
 407 atmospheric heating for DU+WV (green points). Thus the change in sign from cooling due to  
 408 heating (also seen in Figure 5c) for DU+WV compared to DU is explained by lower moisture  
 409 content in the lower-SAL, and the LW ATM DRE for WV increases as moisture in the lower-  
 410 SAL decreases. In Figure 6b, a drier, dustier lower-SAL results in a positive surface DRE for  
 411 DU. Since the WV surface DRE is negative, values for DU+WV are sometimes large enough to  
 412 change the sign compared to DU. In contrast the TOA DRE shows no dependence on WV in the  
 413 lower SAL in Figure 6a.

414



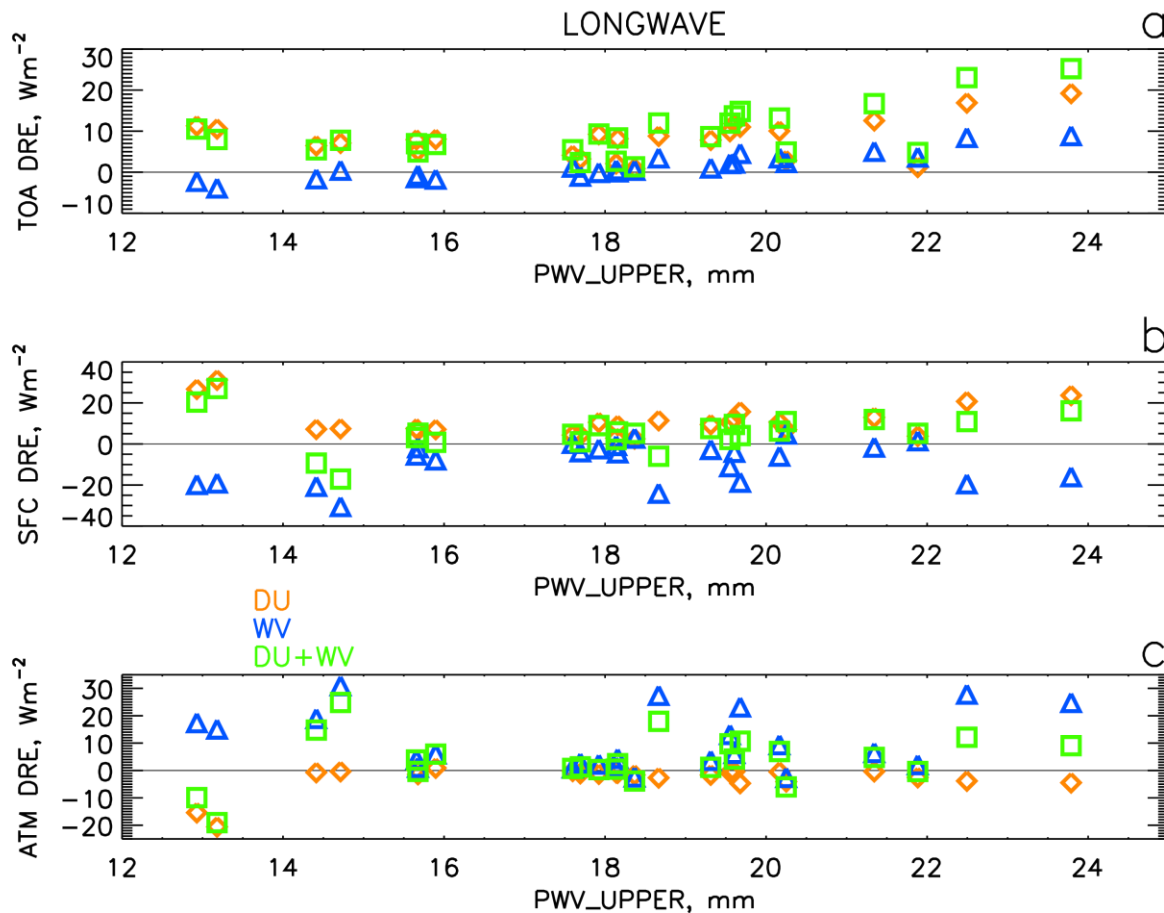
415  
 416 **Figure 7.** Longwave DRE relative to control experiment, as a function of the lower SAL PWV  
 417 (PWV\_lower), for the inclusion of dust only (DU, orange), WV only (blue) and dust and WV  
 418 (DU+WV, green). Panels show (a) DRE at the TOA, (b) surface and (c) atmospheric column.

419 Figure 8 shows the DREs as a function of PWV in the upper-SAL. Although PWV\_upper has no  
 420 observable effect over the LW DRE at the surface and on the total atmospheric column, it has a  
 421 strong effect on the LW DRE at the TOA. Larger PWV\_upper (associated with increased

422 dustiness) results in larger, more positive LW TOA DREs due to reduced outgoing longwave  
 423 radiation. This is seen for both the WV and DU experiments. When WV in the upper-SAL is  
 424 higher, its proximity to the TOA (compared to the lower SAL) means that enhanced upper-SAL  
 425 WV results in less LW radiation being emitted and therefore a warming effect results. At the  
 426 same time, since dust AOD and PWV\_upper are related, the LW dust TOA DRE also increases  
 427 for high PWV\_upper values. As a result, the two effects act in the same direction and increase  
 428 the DU+WV TOA DRE.

429

430 This also explains the trend seen in Figure 5a, and confirms that the TOA WV effect is  
 431 controlled by changes to PWV\_upper, rather than PWV\_lower. Thus increases in dust and  
 432 increased PWV\_upper both act to cause and amplify a positive LW TOA DRE.  
 433



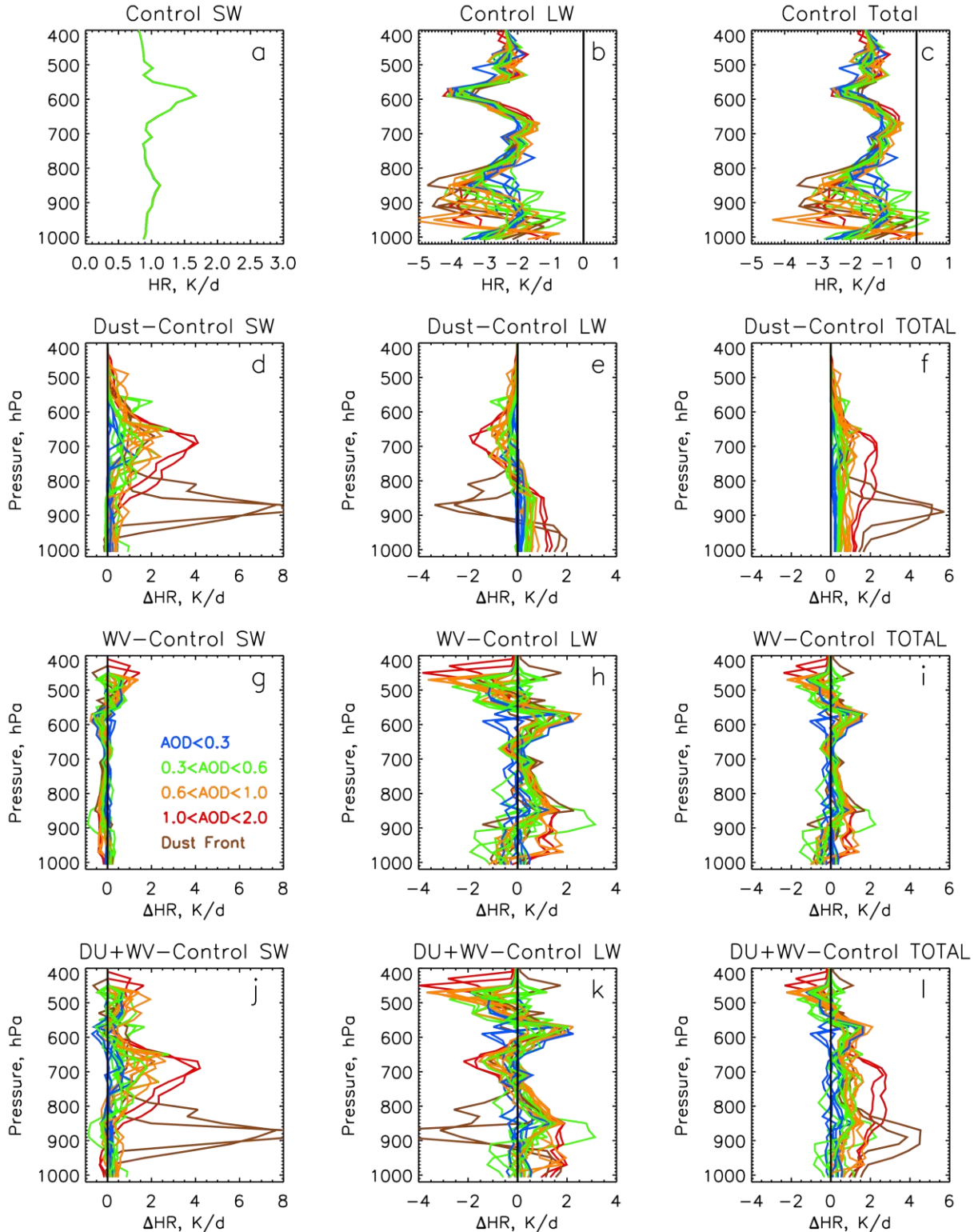
434

435 **Figure 8.** Longwave DRE relative to control experiment, as a function of the upper SAL PWV  
 436 (PWV\_upper), for the inclusion of dust only (DU, orange), WV only (blue) and dust and WV  
 437 (DU+WV, green). Panels show (a) DRE at the TOA, (b) surface and (c) atmospheric column.

438 Figure 9 shows the absolute heating rates for the control and changes in heating rates for each  
 439 experiment for the SW, LW and total relative to the control. It can be seen that dust (Figure 9 d-  
 440 f) causes a SW heating, a LW cooling, and an total heating. In the SW, WV (Figure 9g) causes a  
 441 slight heating at higher altitudes which is stronger and higher for larger AOD where PWV\_upper  
 442 is larger. In the LW (panel h), the impact of increased PWV\_upper and decreased PWV\_lower

443 can be seen. When AODs are higher, more upper-SAL cooling from enhanced moisture and less  
444 mid-SAL cooling (i.e. warming) from enhanced dryness is observed. This results in changes to  
445 total heating rates of up to -2.5 K/d in the upper SAL and +1.5 K/d through the lower-SAL due  
446 to the dust-related WV changes (panel i).

447  
448 Comparing Fig f to Fig l shows the changes in total heating rates due to DU+WV compared to  
449 dust alone. We see that the total WV+DU heating rates (fig l) show extra cooling at heights  
450 above 550 hPa and increased heating through the mid-SAL (~950 to 600 hPa), higher by about 2  
451 K/d relative to Fig f . Although increased dust was associated with decreased PWV\_lower at  
452 heights beneath 820 hPa, the radiative heating effects of this WV change are felt throughout the  
453 wider column up to around 680 hPa. As a result, the PWV\_lower changes control the ATM  
454 DRE, determining atmospheric heating or cooling, as shown in Figure 6c. It is also notable that  
455 only by including the enhanced WV in the upper SAL, is the cold anomaly in potential  
456 temperatures seen in Figure 3d consistent with the additional cooling rates above around 500  
457 hPa.  
458



459  
460  
461  
462

**Figure 9.** Top row: absolute heating rates for the CONTROL for all profiles for (a) SW, (b) LW, (c) total (SW+LW). Other rows: changes in heating rates (HR, K/day) between each experiment and the control, for (d-f) DU, (g-i) WV (middle row) and (j-l) WV+DU (bottom row), for the SW

463 spectrum (left), LW spectrum (center) and total (SW plus LW, right). Profiles are colored as a  
464 function of AOD.

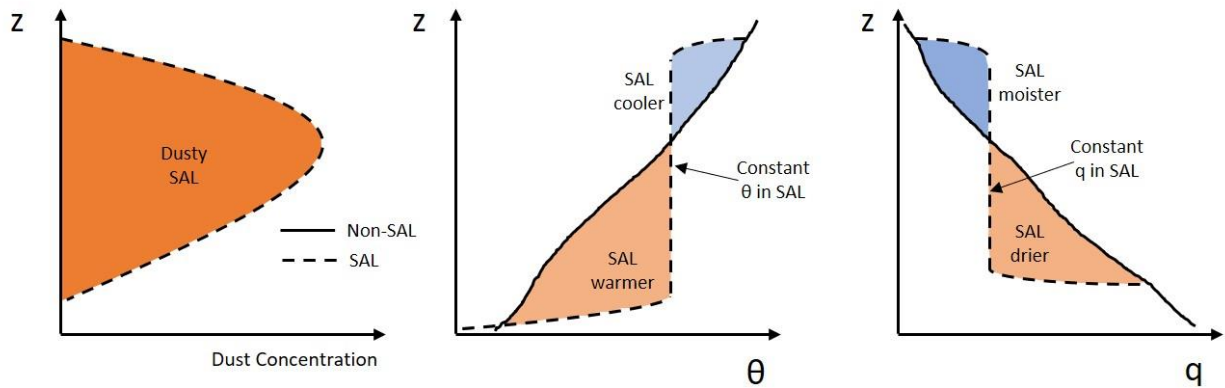
#### 465 **4 Discussion**

466 This work finds elevated moisture levels in the upper SAL associated with dust, and  
467 demonstrates that this increased moisture is important in determining the magnitude, and  
468 potentially the sign of the radiative effect exerted by the dusty SAL. The elevated moisture found  
469 in the upper SAL differs to the frequently reported SAL characteristics of it being a  
470 straightforward dry layer, suggesting that more complexity and vertical detail is required to  
471 accurately reflect the SAL and its radiative impacts.

472  
473 Much previous work characterizing the SAL focuses on the its lower atmospheric structure,  
474 particularly heating rates at around 850 hPa and their relation to sustaining the temperature  
475 inversion between the marine boundary layer and the SAL base, due to its importance in  
476 suppression of convection and potentially impeding tropical cyclone development (e.g. Dunion  
477 and Velden (2004); Wong et al. (2009)). However, a few studies have focused more on the  
478 structure of the entire depth of the SAL. For example, Braun (2010) find a 400-600hPa  
479 moistening across Africa to Saudi Arabia relative to the very dry Saharan air below, due to deep,  
480 dry convective mixing over the Sahara. This structure has sometimes been found at the west  
481 coast of Africa and also downstream. Ismail et al. (2010) show a case where WV mixing ratios  
482 were around 2 to 7 g/kg throughout the SAL. They attribute this increased moisture to  
483 midaltitude convection as a result of intensification of an AEW, pointing out that increased WV  
484 leaves the SAL more amenable to convection. Thus the elevated WV in the upper SAL may have  
485 a wider dynamical impact than has been possible to examine here.

486  
487 Despite the fact that the observations presented here show enhanced moisture in the upper-SAL  
488 compared to background conditions, we do not suggest that the SAL is not a well-mixed,  
489 elevated layer. This is illustrated through the schematic shown in Figure 10, which is based on  
490 the observations shown in Figure 3. The background (non-SAL) profiles of potential temperature  
491 and water vapor mixing ratio are represented by gradually increasing and decreasing values,  
492 respectively. Therefore, when a well-mixed layer (the SAL), with near-constant potential  
493 temperature and water vapor mixing ratio, is imposed, this results in either a positive or negative  
494 anomaly in both its upper and lower portions. Therefore, the results presented in this work do not  
495 oppose the previous documentation of the SAL evidencing its well-mixed nature, they simply  
496 expose the extension of the well-mixed SAL upwards which results in the cooler, moister  
497 anomalies shown in Figure 10. The absolute magnitude of water vapor mixing ratios in the SAL  
498 will determine the magnitude of the anomalies relative to the background condition, such that a  
499 moister, well-mixed SAL will shift the line of constant  $q$  shown in Figure 10 to the right,  
500 increasing the moist anomaly.

501



502  
 503 **Figure 10:** Schematic depicting anomalies observed in the dusty SAL. SAL conditions are  
 504 characterized by well-mixed, elevated potential temperature ( $\theta$ ) and water vapor mixing ratios  
 505 ( $q$ ). Compared to the background, non-SAL environment, this results in a warmer, drier lower-  
 506 SAL and a cooler, moister upper-SAL.

507 Gutleben et al. (2019) present airborne observations from a case study in the western Atlantic  
 508 SAL. Although they find that WV mixing ratios increased in the SAL relative to the free  
 509 troposphere, their figures show that the SAL was actually drier than the tropical standard  
 510 atmosphere. Nevertheless, their results show that the increase from dry to moist air descending  
 511 into the top of the SAL was important for driving strong LW cooling rates at the top of the SAL,  
 512 similar to the heating rate profiles shown here.

513  
 514 Adebisi et al. (2015) present similar findings to this work, but for biomass burning aerosol  
 515 (BBA) layers over the southeast Atlantic containing enhanced moisture. They find that this  
 516 anomalous moisture leads to anomalous LW cooling in the layer counteracting the SW heating  
 517 from the BBA. However, due to the negligible LW radiative effect of BBA, the LW and SW  
 518 radiative effects of WV combine differently in the results of Adebisi et al. (2015) to those  
 519 presented here. Clearly dust layers are not the only type of aerosol layer which can be collocated  
 520 with enhanced WV, and there may be more instances of transported aerosol layers globally  
 521 where WV changes exert an effect.

522  
 523 As well as influencing the radiative effect, enhanced upper SAL moisture and associated cooling  
 524 at these altitudes may also influence mid-level altocumulus cloud development. For example, it  
 525 could be important to the development of the frequently observed altocumulus cloud capping the  
 526 SABL and SAL, as shown in Kealy et al. (2017) and Mantsis et al. (2020), which play an  
 527 important radiative role.

528  
 529 The additional cooling at the top of the SAL due to WV may help to maintain its well-mixed  
 530 vertical structure, aiding subsidence at the SAL top, combined with ascent at the SAL base due  
 531 to the well-known lower SAL heating from both dust and water vapor. This is consistent with a  
 532 lowering of the SAL top towards the west, and a rising of the SAL base (e.g. Liu et al. (2008),  
 533 Tsamalis et al. (2013)).

534  
 535 An interesting question regarding elevated moisture in the upper SAL is whether this is a feature  
 536 that has simply been under-investigated in the past, or whether the moistening is a temporal

537 trend. Evan et al. (2015) show that WV content in the Saharan heat low region over Africa has  
538 increased over the last 30 years as a result of a WV-temperature feedback cycle. Thus it seems  
539 plausible that the SAL, outflowing from the Sahara, may be moistening as a consequence. Cold  
540 pool outflows (haboobs) play a key role in the transport of both water vapor and dust into the  
541 Saharan heat low region (Allen et al., 2013; Engelstaedter et al., 2015; Flamant et al., 2007;  
542 Marsham et al., 2013; Yu et al., submitted) where it is mixed throughout the deep Saharan  
543 boundary layer with dust, before being transported westwards as the SAL. Therefore another  
544 question which arises is whether the intensity and/or frequency of cold pool outflows over west  
545 Africa has changed over time.

546  
547 The ability of enhanced moisture in the upper-SAL to reduce the magnitude of the negative TOA  
548 radiative effect of the SAL, shifting it towards positive values, is particularly important when  
549 considered with other recent developments in the literature. Adebisi and Kok (2020) have shown  
550 that climate models miss most coarse dust in the atmosphere, and including this missed coarse  
551 dust adds a TOA radiative warming effect of  $0.15 \text{ Wm}^{-2}$  globally. Di Biagio et al. (2020) show  
552 that updated dust optical properties and inclusion of dust sizes larger than  $20 \mu\text{m}$  further shifts  
553 the global direct radiative effect of dust away from a cooling effect, to  $-0.03 \text{ Wm}^{-2}$ . When  
554 combined with potential increases in upper SAL moisture, this will further shift the regional  
555 radiative effect of dust towards a net warming effect over the tropical Atlantic. The importance  
556 of these combined effects will be further increased in regions where dust emissions are  
557 increasing over time, exerting a radiative forcing which may tend towards positive values.

558  
559 Another pertinent question concerns potential mechanisms which may enable coarse dust  
560 particles to be transported further than expected (Mallios et al., 2020; O'Sullivan et al., 2020;  
561 Ryder et al., 2019; van der Does et al., 2018; Weinzierl et al., 2017). This work shows that as  
562 well as a significant day-time shortwave atmospheric column heating from dust, the reduced  
563 lower-SAL moisture which occurs under dustier conditions can lead to increased atmospheric  
564 longwave heating throughout most of the SAL depth, which would dominate at night. Both these  
565 mechanisms may contribute to upward dynamic effects which may increase the lifetime and  
566 long-range transport of dust particles, including the coarser sizes.

567  
568 Finally there are several uncertainties and limitations inherent in this work. Firstly, the  
569 observations, although constituting 24 profiles over the course of 19 days and 5 dust events, are  
570 only representative of August 2015 and the eastern Tropical Atlantic, and a wider spatial and  
571 temporal analysis would be beneficial. For example, questions such as whether the upper-SAL  
572 WV enhancement is present throughout the summer dust season, and how this may vary year to  
573 year and westwards across the Atlantic are important.

574  
575 The main uncertainty in this work stems from the optical properties of the dust applied in the  
576 RTM, which were setup specifically to match the in-situ size and composition results measured  
577 during the AER-D campaign (Ryder et al., 2018). As a sensitivity study, optical properties were  
578 also selected to represent more extreme values of absorbing dust and less absorbing dust. The  
579 impact of the WV perturbation to the DRE is quite sensitive to the optical properties assumed.  
580 For example, at the TOA, the total DRE due to dust approaches zero when dust is very absorbing  
581 in the SW. Therefore, when the WV changes are also included, which are positive, the final TOA  
582 DRE from DU+WV can sometimes change sign, becoming positive. Conversely, for less

583 absorbing dust with a high SSA, the dust DRE at the TOA is more negative. Therefore,  
584 proportionally the addition of a positive WV DRE results in a smaller fractional decrease in the  
585 negative DRE. Nevertheless, whatever the chosen optical properties of dust are, the radiative  
586 changes due to the WV profile remain important.

587  
588 Finally, this work does not account for any changes in humidity upon the microphysical  
589 properties of the dust, such as possible hydrophilic growth and changes in scattering properties.  
590 Although it is possible that hydrophobic dust particles become more hydrophilic during transport  
591 through chemical coatings such as sulfate, there is much uncertainty in understanding of this  
592 process and some studies show that this is not an important factor during trans-Atlantic dust  
593 transport (Denjean et al., 2015). Additionally, measurements of scattering and absorption at  
594 different humidities were not taken during AER-D.  
595

## 596 **5 Conclusions**

597 This work presents results from 24 in-situ aircraft profiles from 5 dust events over the eastern  
598 tropical Atlantic during August 2015. It has been shown that as dust loadings increase and the  
599 thermal characteristics of the SAL develop, WV mixing ratios decrease in the lower-SAL ( $p > 820$   
600 hPa) and increase in the upper SAL (480 hPa to 780 hPa) at a mean rate of 3.8 mm per unit  
601 AOD.

602  
603 Conventionally the SAL is considered to be a warm, dry, elevated, well-mixed layer which is  
604 frequently dusty (e.g. Carlson and Prospero (1972)). Therefore the observations of enhanced  
605 moisture in the upper SAL under dusty conditions are somewhat contradictory to this  
606 description. This can be reconciled by observations presented here showing that the SAL has  
607 well-mixed characteristics, but by extending them in altitude where the SAL then becomes  
608 cooler and moister than the background conditions.

609  
610 The radiative impact of the observed WV and dusty profiles has been quantified using a radiative  
611 transfer model. The enhanced upper-SAL moisture was found to have most effect at the TOA,  
612 causing a positive DRE, counteracting the negative TOA DRE exerted by the dust. When both  
613 WV and dust were included, the negative DRE at the TOA from dust was reduced in magnitude  
614 by up to 64% with a mean of 11%. Thus, accounting for the complex WV profile is crucial in  
615 determining the radiative effect of the dusty SAL, and is significantly different to simply  
616 assuming a dry profile.

617  
618 The total DRE at the surface and in the atmosphere were dominated by dust effects, but were  
619 enhanced by WV reductions in the lower-SAL. Decreases in lower-SAL WV acted to increase  
620 the negative surface DRE from dust by 8% and increase atmospheric heating by 17% on average.

621  
622 Changes in in the total DRE were driven by WV changes from the longwave spectrum. Less WV  
623 in the lower-SAL under dusty conditions resulted in a more negative surface LW DRE due to  
624 less emission of LW radiation from WV towards the surface from the lower-SAL. At the same  
625 time, less LW cooling occurred in the drier lower-SAL due to smaller LW absorption. In the LW  
626 spectrum, the inclusion of the dry lower-SAL results in change in sign from net cooling to net

627 heating compared to dust only, and could be important for nighttime dynamics and dust transport  
628 within the SAL.

629  
630 Heating rate profile changes due to WV and dust in the SAL were calculated. Dust was found to  
631 cause a net heating, driven by SW heating, whereas the WV structure generated cooling in the  
632 upper-SAL and heating throughout the mid to lower-SAL compared to background conditions,  
633 amplifying the heating occurring here due to dust. The upper-SAL cooling under dustier  
634 conditions due to WV is consistent with colder upper SAL temperatures in dusty conditions.

635  
636 Although this work only represents dust events in the SAL from August 2015, increased  
637 moisture in the SAL is consistent with an observed moistening of the Saharan heat low region  
638 over west Africa over the last 30 years as part of a feedback cycle driven by increased  
639 temperatures (Evan et al., 2015). Cold pool outflows play a crucial role in transporting WV into  
640 the Saharan heat low region (Allen et al., 2013; Engelstaedter et al., 2015; Flamant et al., 2007;  
641 Marsham et al., 2013). Therefore future work should evaluate the prevalence of moisture on  
642 wider temporal and spatial scales than has been possible here, and also examine whether there  
643 are temporal trends in the transport of WV and dust northwards into the Sahara by cold pool  
644 outflows, potentially as a result of climate change, as well as examining the ability of models  
645 with explicit dust schemes to reproduce the dust-WV relationship shown here.

646

#### 647 **Acknowledgments**

648 C.L.Ryder received funding from NERC Independent Research Fellowship NE/M018288/1.  
649 Airborne data from the BAe 146 were obtained using the BAe 146-301 Atmospheric Research  
650 Aircraft operated by Directflight Ltd and managed by FAAM, which was a joint entity of the  
651 NERC and the UK Met Office. Keith Shine, Ross Herbert and Franco Marengo are thanked for  
652 useful discussions relating to this work.

#### 653 **Data**

654 Aircraft data is available at the Centre for Environmental Data Archive at:  
655 <http://catalogue.ceda.ac.uk/uuid/d7e02c75191a4515a28a208c8a069e70>

#### 656 **References**

- 657  
658 Adebisi, A. A., & Kok, J. F. (2020). Climate models miss most of the coarse dust in the  
659 atmosphere. *Science Advances*, 6(15). doi:10.1126/sciadv.aaz9507  
660 Adebisi, A. A., Zuidema, P., & Abel, S. J. (2015). The Convolution of Dynamics and Moisture  
661 with the Presence of Shortwave Absorbing Aerosols over the Southeast Atlantic. *Journal*  
662 *of Climate*, 28(5), 1997-2024. doi:10.1175/Jcli-D-14-00352.1  
663 Allen, C. J. T., Washington, R., & Engelstaedter, S. (2013). Dust emission and transport  
664 mechanisms in the central Sahara: Fennec ground-based observations from Bordj Badji  
665 Mokhtar, June 2011. *Journal of Geophysical Research-Atmospheres*, 118(12), 6212-  
666 6232. doi:10.1002/jgrd.50534  
667 Anderson, G. P., Clough, S. A., Kneizys, F. X., Chetwynd, J. H., & Shettle, E. P. (1986). *AFGL*  
668 *atmospheric constituent profiles (0-120 km)*, Technical Report AFGL-TR-86-0110, AFGL  
669 (OPI), Hanscom. (AFB, MA. 01736). Retrieved from

- 670 Balkanski, Y., Schulz, M., Claquin, T., & Guibert, S. (2007). Reevaluation of Mineral aerosol  
 671 radiative forcings suggests a better agreement with satellite and AERONET data.  
 672 *Atmospheric Chemistry and Physics*, 7, 81-95.
- 673 Braun, S. A. (2010). Reevaluating the Role of the Saharan Air Layer in Atlantic Tropical  
 674 Cyclogenesis and Evolution. *Monthly Weather Review*, 138(6), 2007-2037.  
 675 doi:10.1175/2009mwr3135.1
- 676 Carlson, T. N. (2016). The Saharan Elevated Mixed Layer and its Aerosol Optical Depth. *The*  
 677 *Open Atmospheric Science Journal*, 10, 26-38. doi:DOI: 10.2174/1874282301610010026
- 678 Carlson, T. N., & Benjamin, S. G. (1980). Radiative Heating Rates for Saharan Dust. *Journal of*  
 679 *the Atmospheric Sciences*, 37(1), 193-213. doi:Doi 10.1175/1520-  
 680 0469(1980)037<0193:Rhrfsd>2.0.Co;2
- 681 Carlson, T. N., & Prospero, J. (1972). The Large-Scale Movement of Saharan Air Outbreaks  
 682 over the Northern Equatorial Atlantic. *Journal of Applied Meteorology and Climatology*,  
 683 11(2), 283-297. doi:[https://doi.org/10.1175/1520-  
 684 0450\(1972\)011<0283:TLSMOS>2.0.CO;2](https://doi.org/10.1175/1520-0450(1972)011<0283:TLSMOS>2.0.CO;2)
- 685 Colarco, P. R., Nowottnick, E. P., Randles, C. A., Yi, B. Q., Yang, P., Kim, K. M., . . . Bardeen,  
 686 C. G. (2014). Impact of radiatively interactive dust aerosols in the NASA GEOS-5  
 687 climate model: Sensitivity to dust particle shape and refractive index. *Journal of*  
 688 *Geophysical Research-Atmospheres*, 119(2), 753-786. doi:10.1002/2013jd020046
- 689 Cusack, S., Edwards, J. M., & Crowther, J. M. (1999). Investigating k distribution methods for  
 690 parameterizing gaseous absorption in the Hadley Centre Climate Model. *Journal of*  
 691 *Geophysical Research-Atmospheres*, 104(D2), 2051-2057. doi:Doi  
 692 10.1029/1998jd200063
- 693 Denjean, C., Caquineau, S., Desboeufs, K., Laurent, B., Maille, M., Rosado, M. Q., . . .  
 694 Formenti, P. (2015). Long-range transport across the Atlantic in summertime does not  
 695 enhance the hygroscopicity of African mineral dust. *Geophysical Research Letters*,  
 696 42(18), 7835-7843. doi:10.1002/2015gl065693
- 697 Di Biagio, C., Balkanski, Y., Albani, S., Boucher, O., & Formenti, P. (2020). Direct Radiative  
 698 Effect by Mineral Dust Aerosols Constrained by New Microphysical and Spectral Optical  
 699 Data. *Geophysical Research Letters*, 47(2). doi:10.1029/2019GL086186
- 700 Doherty, O. M., & Evan, A. T. (2014). Identification of a new dust-stratocumulus indirect effect  
 701 over the tropical North Atlantic. *Geophysical Research Letters*, 41(19), 6935-6942.  
 702 doi:10.1002/2014gl060897
- 703 Dubovik, O., Holben, B., Eck, T. F., Smirnov, A., Kaufman, Y. J., King, M. D., . . . Slutsker, I.  
 704 (2002). Variability of absorption and optical properties of key aerosol types observed in  
 705 worldwide locations. *Journal of the Atmospheric Sciences*, 59(3), 590-608. doi:Doi  
 706 10.1175/1520-0469(2002)059<0590:Voaaop>2.0.Co;2
- 707 Dunion, J. P. (2011). Rewriting the Climatology of the Tropical North Atlantic and Caribbean  
 708 Sea Atmosphere. *Journal of Climate*, 24(3), 893-908. doi:10.1175/2010jcli3496.1
- 709 Dunion, J. P., & Velden, C. S. (2004). The impact of the Saharan air layer on Atlantic tropical  
 710 cyclone activity. *Bulletin of the American Meteorological Society*, 85(3), 353-+. doi:Doi  
 711 10.1175/Bams-85-3-353
- 712 Edwards, J. M., & Slingo, A. (1996). Studies with a flexible new radiation code .1. Choosing a  
 713 configuration for a large-scale model. *Quarterly Journal of the Royal Meteorological*  
 714 *Society*, 122(531), 689-719.

- 715 Engelstaedter, S., Washington, R., Flamant, C., Parker, D. J., Allen, C. J. T., & Todd, M. C.  
716 (2015). The Saharan heat low and moisture transport pathways in the central Sahara-  
717 Multi-aircraft observations and Africa-LAM evaluation. *Journal of Geophysical*  
718 *Research-Atmospheres*, 120(10), 4417-4442. doi:10.1002/2015jd023123
- 719 Evan, A. T., Flamant, C., Lavaysse, C., Kocha, C., & Saci, A. (2015). Water Vapor-Forced  
720 Greenhouse Warming over the Sahara Desert and the Recent Recovery from the Sahelian  
721 Drought. *Journal of Climate*, 28(1), 108-123. doi:10.1175/Jcli-D-14-00039.1
- 722 Flamant, C., Chaboureaud, J. P., Parker, D. J., Taylor, C. A., Cammas, J. P., Bock, O., . . . Pelon,  
723 J. (2007). Airborne observations of the impact of a convective system on the planetary  
724 boundary layer thermodynamics and aerosol distribution in the inter-tropical  
725 discontinuity region of the West African Monsoon. *Quarterly Journal of the Royal*  
726 *Meteorological Society*, 133(626), 1175-1189. doi:Doi 10.1002/Qj.97
- 727 Gutleben, M., Gross, S., Wirth, M., Emde, C., & Mayer, B. (2019). Impacts of Water Vapor on  
728 Saharan Air Layer Radiative Heating. *Geophysical Research Letters*, 46(24), 14854-  
729 14862. doi:10.1029/2019gl085344
- 730 Hess, M., Koepke, P., & Schult, I. (1998). Optical properties of aerosols and clouds: The  
731 software package OPAC. *Bulletin of the American Meteorological Society*, 79(5), 831-  
732 844. doi:Doi 10.1175/1520-0477(1998)079<0831:Opoaac>2.0.Co;2
- 733 Ismail, S., Ferrare, R. A., Browell, E. V., Kooi, S. A., Dunion, J. P., Heymsfield, G., . . .  
734 Anderson, B. (2010). LASE Measurements of Water Vapor, Aerosol, and Cloud  
735 Distributions in Saharan Air Layers and Tropical Disturbances. *Journal of the*  
736 *Atmospheric Sciences*, 67(4), 1026-1047. doi:10.1175/2009jas3136.1
- 737 Kanitz, T., Engelmann, R., Heinold, B., Baars, H., Skupin, A., & Ansmann, A. (2014). Tracking  
738 the Saharan Air Layer with shipborne lidar across the tropical Atlantic. *Geophysical*  
739 *Research Letters*, 41(3), 1044-1050. doi:10.1002/2013gl058780
- 740 Karyampudi, V. M., Palm, S. P., Reagen, J. A., Fang, H., Grant, W. B., Hoff, R. M., . . . Melfi, S.  
741 H. (1999). Validation of the Saharan dust plume conceptual model using lidar, Meteosat,  
742 and ECMWF data. *Bulletin of the American Meteorological Society*, 80(6), 1045-1075.
- 743 Kealy, J. C., Marenco, F., Marsham, J. H., Garcia-Carreras, L., Francis, P. N., Cooke, M. C., &  
744 Hocking, J. (2017). Clouds over the summertime Sahara: an evaluation of Met Office  
745 retrievals from Meteosat Second Generation using airborne remote sensing. *Atmospheric*  
746 *Chemistry and Physics*, 17(9), 5789-5807. doi:10.5194/acp-17-5789-2017
- 747 Korolev, A. V., Strapp, J. W., Isaac, G. A., & Nevzorov, A. N. (1998). The Nevzorov airborne  
748 hot-wire LWC-TWC probe: Principle of operation and performance characteristics.  
749 *Journal of Atmospheric and Oceanic Technology*, 15(6), 1495-1510. doi:Doi  
750 10.1175/1520-0426(1998)015<1495:Tnahwl>2.0.Co;2
- 751 Liu, D. T., Taylor, J., Crosier, J., Marsden, N., Bower, K. N., Lloyd, G., . . . Choulaton, T. W.  
752 (2018). Aircraft and ground measurements of dust aerosols over the west African coast in  
753 summer 2015 during ICE-D and AER-D. *Atmospheric Chemistry and Physics*, 18(5),  
754 3817-3838. doi:10.5194/acp-18-3817-2018
- 755 Liu, Z. Y., Omar, A., Vaughan, M., Hair, J., Kittaka, C., Hu, Y. X., . . . Pierce, R. (2008).  
756 CALIPSO lidar observations of the optical properties of Saharan dust: A case study of  
757 long-range transport. *Journal of Geophysical Research-Atmospheres*, 113(D7). doi:Doi  
758 10.1029/2007jd008878

- 759 Mallios, S. A., Drakaki, E., & Amiridis, V. (2020). Effects of dust particle sphericity and  
760 orientation on their gravitational settling in the earth's atmosphere. *Journal of Aerosol*  
761 *Science*, 150. doi:10.1016/j.jaerosci.2020.105634
- 762 Manners, J., Edwards, J., Hill, P., & Thelen, J.-C. (2017). *SOCRATES Technical Guide Suite Of*  
763 *Community RAdiative Transfer codes based on Edwards and Slingo*. Retrieved from  
764 Exeter:
- 765 Mantsis, D. F., Sherwood, S., Dixit, V., Morrison, H., & Thompson, G. (2020). Mid-level clouds  
766 over the Sahara in a convection-permitting regional model. *Climate Dynamics*, 54(7-8),  
767 3425-3439. doi:10.1007/s00382-020-05188-4
- 768 Marengo, F., Ryder, C., Estelles, V., O'Sullivan, D., Brooke, J., Orgill, L., . . . Gallagher, M.  
769 (2018). Unexpected vertical structure of the Saharan Air Layer and giant dust particles  
770 during AER-D. *Atmospheric Chemistry and Physics*, 18(23), 17655-17668.  
771 doi:10.5194/acp-18-17655-2018
- 772 Marsham, J. H., Hobby, M., Allen, C. J. T., Banks, J. R., Bart, M., Brooks, B. J., . . .  
773 Washington, R. (2013). Meteorology and dust in the central Sahara: Observations from  
774 Fennec supersite-1 during the June 2011 Intensive Observation Period. *Journal of*  
775 *Geophysical Research-Atmospheres*, 118(10), 4069-4089. doi:10.1002/jgrd.50211
- 776 Marsham, J. H., Parker, D. J., Grams, C. M., Taylor, C. M., & Haywood, J. M. (2008). Uplift of  
777 Saharan dust south of the intertropical discontinuity. *Journal of Geophysical Research-*  
778 *Atmospheres*, 113(D21). doi:Doi 10.1029/2008jd009844
- 779 Marsham, J. H., Parker, D. J., Todd, M. C., Banks, J. R., Brindley, H. E., Garcia-Carreras, L., . . .  
780 Ryder, C. L. (2016). The contrasting roles of water and dust in controlling daily  
781 variations in radiative heating of the summertime Saharan heat low. *Atmospheric*  
782 *Chemistry and Physics*, 16(5), 3563-3575. doi:10.5194/acp-16-3563-2016
- 783 O'Sullivan, D., Marengo, F., Ryder, C. L., Pradhan, Y., Kipling, Z., Johnson, B., . . . Selmer, P.  
784 (2020). Models transport Saharan dust too low in the atmosphere: a comparison of the  
785 MetUM and CAMS forecasts with observations. *Atmospheric Chemistry and Physics*,  
786 20(21), 12955-12982. doi:10.5194/acp-20-12955-2020
- 787 Prospero, J. M., & Carlson, T. N. (1972). Vertical and Areal Distribution of Saharan Dust over  
788 Western Equatorial North-Atlantic Ocean. *Journal of Geophysical Research*, 77(27),  
789 5255-&. doi:DOI 10.1029/JC077i027p05255
- 790 Randles, C., Kinne, S., Myhre, G., Schulz, M., Stier, P., Fischer, J., . . . Lu, P. (2012).  
791 Intercomparison of shortwave radiative transfer schemes in global aerosol modeling:  
792 Results from the AeroCom Radiative Transfer Experiment. *Atmos. Chem. Phys. Discuss.*,  
793 12(12), 32631-32706. doi:doi:10.5194/acpd-12-32631-2012
- 794 Rothman, L. S., Barbe, A., Benner, D. C., Brown, L. R., Camy-Peyret, C., Carleer, M. R., . . .  
795 Yoshino, K. (2003). The HITRAN molecular spectroscopic database: edition of 2000  
796 including updates through 2001. *Journal of Quantitative Spectroscopy & Radiative*  
797 *Transfer*, 82(1-4), 5-44. doi:10.1016/S0022-4073(03)00146-8
- 798 Ryder, C. L., Highwood, E. J., Walser, A., Seibert, P., Philipp, A., & Weinzierl, B. (2019).  
799 Coarse and giant particles are ubiquitous in Saharan dust export regions and are  
800 radiatively significant over the Sahara. *Atmospheric Chemistry and Physics*, 19(24),  
801 15353-15376. doi:10.5194/acp-19-15353-2019
- 802 Ryder, C. L., Marengo, F., Brooke, J. K., Estelles, V., Cotton, R., Formenti, P., . . . Murray, B. J.  
803 (2018). Coarse-mode mineral dust size distributions, composition and optical properties

- 804 from AER-D aircraft measurements over the tropical eastern Atlantic. *Atmospheric*  
805 *Chemistry and Physics*, 18(23), 17225-17257. doi:10.5194/acp-18-17225-2018
- 806 Tsamalis, C., Chedin, A., Pelon, J., & Capelle, V. (2013). The seasonal vertical distribution of  
807 the Saharan Air Layer and its modulation by the wind. *Atmospheric Chemistry and*  
808 *Physics*, 13(22), 11235-11257. doi:10.5194/acp-13-11235-2013
- 809 van der Does, M., Knippertz, P., Zschenderlein, P., Harrison, R. G., & Stuut, J. B. W. (2018).  
810 The mysterious long-range transport of giant mineral dust particles. *Science Advances*,  
811 4(12). doi:10.1126/sciadv.aau2768
- 812 Volz, F. E. (1973). Infrared Optical-Constants of Ammonium Sulfate, Sahara Dust, Volcanic  
813 Pumice, and Flyash. *Applied Optics*, 12(3), 564-568. doi:Doi 10.1364/Ao.12.000564
- 814 Walters, D. N., Best, M. J., Bushell, A. C., Copsey, D., Edwards, J. M., Falloon, P. D., . . .  
815 Williams, K. D. (2011). The Met Office Unified Model Global Atmosphere 3.0/3.1 and  
816 JULES Global Land 3.0/3.1 configurations. *Geoscientific Model Development*, 4(4), 919-  
817 941. doi:10.5194/gmd-4-919-2011
- 818 Weinzierl, B., Ansmann, A., Prospero, J. M., Althausen, D., Benker, N., Chouza, F., . . . Walser,  
819 A. (2017). The Saharan Aerosol Long-range Transport and Aerosol-cloud-interaction  
820 experiment: Overview and Selected Highlights. *Bulletin of the American Meteorological*  
821 *Society*, 98(7), 1427-1451. doi:10.1175/Bams-D-15-00142.1
- 822 Wong, S., & Dessler, A. E. (2005). Suppression of deep convection over the tropical North  
823 Atlantic by the Saharan Air Layer. *Geophysical Research Letters*, 32(9).  
824 doi:10.1029/2004gl022295
- 825 Wong, S., Dessler, A. E., Mahowald, N. M., Yang, P., & Feng, Q. (2009). Maintenance of Lower  
826 Tropospheric Temperature Inversion in the Saharan Air Layer by Dust and Dry Anomaly.  
827 *Journal of Climate*, 22(19), 5149-5162. doi:10.1175/2009jcli2847.1
- 828 Yu, H., Tan, Q., Zhou, L., Bian, H. S., Chin, M., Ryder, C. L., . . . Holben, B. (submitted).  
829 Observation and modeling of a gigantic African dust intrusion into the Caribbean Basin  
830 and the southern U.S. in June 2020. *Atmos. Chem. Phys.*
- 831 Zdunkowski, W. G., Welch, R. M., & Korb, G. (1980). An investigation of the structure of  
832 typical two-stream methods for the calculation of solar fluxes and heating rates in clouds.  
833 *Beiträge Phys. Atmosph.*, 53, 147-166.  
834